Scientific Reports
https://doi.org/10.1038/s41598-026-62405-6

Article in Press

High Q-factor multiband terahertz metasurface biosensor for biomedical refractive index sensing: a numerical study

Received: 24 April 2026
Accepted: 10 July 2026
Published online: 19 July 2026

Cite this article as: Amer A.A.G., Aladadi Y.T., Sali A. *et al.* High Q-factor multiband terahertz metasurface biosensor for biomedical refractive index sensing: a numerical study. *Sci Rep* (2026). https://doi.org/10.1038/s41598-026-62405-6

Abdulrahman Ahmed Ghaleb Amer, Yosef T. Aladadi, Aduwati Sali, Shaiful Jahari Hashim, Ali Ahmed Salem, Zaid Ahmed Shamsan, Muhammad Zamir Mohyedin & A. J. A. Al-Gburi

High Q-Factor Multiband Terahertz Metasurface Biosensor for Biomedical Refractive Index Sensing: A Numerical Study

Abdulrahman Ahmed Ghaleb Amer[1,3*], Yosef T. Aladadi[2], Aduwati Sali[1&4], Shaiful Jahari Hashim[1&4], Ali Ahmed Salem[5], Zaid Shamsan[2*], Muhammad Zamir Mohyedin[1], and A.J.A. Al-Gubri[6]

[1]Institute for Mathematical Research (INSPEM), Universiti Putra Malaysia (UPM), 43400 Serdang, Selangor, Malaysia.
[2]Department of Electrical Engineering, College of Engineering, Imam Mohammad Ibn Saud Islamic University (IMSIU), Riyadh 11432, Saudi Arabia.
[3]Faculty of Engineering, Department of Electrical Engineering, Sana'a University, Sana'a, Yemen.
[4]WiPNET Research Centre, Department of Computer and Communication Systems Engineering, Faculty of Engineering, Universiti Putra Malaysia (UPM), 43400 Serdang, Selangor, Malaysia.
[5]Interdisciplinary Research Center for Sustainable Energy Systems, King Fahd University of Petroleum & Minerals, Dhahran 31261, Saudi Arabia.
[6] Strategic Research Institute (SRI), Asia Pacific University, Jalan Teknologi 5, Taman Teknologi Malaysia, 57000, Kuala Lumpur, Malaysia
*Corresponding Authors: Abdulrahman A. G. Amer (email: aag2014ye@gmail.com); Zaid Shamsan (email: zashamsan@imamu.edu.sa)

Abstract: Terahertz (THz) metasurface absorbers have emerged as promising platforms for biomedical sensing due to their high-quality (Q) resonances and strong sensitivity to dielectric variations in biological tissues. Conventional single-band designs are effective only over a narrow frequency range, reducing detection reliability and increasing false positives. This study introduces a polarization-independent multiband metasurface absorber (MSA) with good angular stability for label-free terahertz biosensing applications. The structure features a dual-metallic split-ring resonator with a continuous backside ground plane, arranged in a compact metal-dielectric-metal (MDM) pattern. The proposed absorber exhibits six absorption peaks with near-unity (>98%) absorption at 1.80, 2.89, 4.65, 4.84, 5.12, and 5.84 THz. Furthermore, a Q-factor of 177, along with narrow full-width at half-maximum (FWHM) values, ensures exceptional spectral selectivity. The sensor exhibits sensitivities of up to 2.92 THz/RIU and 8 THz/RIU for refractive index ranges corresponding to reported cancer- and malaria-related biological samples, respectively. The resonances enhance light–matter interactions and improve refractive-index sensing performance through stronger electromagnetic field confinement. The proposed design provides a simple, high-Q, multiband platform for THz biosensing applications and is compatible with future microfluidic integration.

Keywords: THz absorber, metasurface, biosensor, cancer detection, malaria detection.

1. INTRODUCTION

THz spectrum, spanning 0.1 to 10 THz, has garnered significant attention for its useful properties, including low photon energy, non-ionizing characteristics, and high sensitivity to molecular vibrations and rotational modes. These unique features enable safe communication with biological tissues and allow distinct biomolecular structures to exhibit their own spectroscopic signatures. As a result, THz technology appears very promising for applications in imaging, material analysis, defense, and biosensing [1], [2]. Metamaterials are artificial materials with structures smaller than the wavelength of light and exhibit properties not found in nature [3]. Their unique characteristics, such as negative permittivity and permeability, enable various uses, including perfect absorbers [4], [5], energy harvesting [6], [7], [8], antennas [9], cloaking [10], sensing [11]–[13], and more. Metamaterial absorbers have attracted considerable attention due to their capacity to attain perfect absorption at designated frequencies. A metamaterial absorber is usually made up of a patterned metallic resonator, a dielectric spacer, and a metallic ground plane that prevents transmission. Also, to get a perfect absorption, it's important to keep the reflection and transmission coefficients as low as possible. The reflection coefficient can be minimized by matching the absorber's input impedance to that of free space. Landy et al. published the first perfect microwave metamaterial absorber in 2008 [14]. Soon after, Tao et al. enhanced this idea for the THz range by adding a narrowband THz metamaterial absorber [15]. This revealed new options for compact, polarization-insensitive, frequency-selective THz devices that absorb more efficiently. However, these improvements reveal a flaw in single-band absorbers: their resonant nature limits absorption to a narrow spectral range, making them less effective outside it. In biosensing and other applications where different biological analytes exhibit distinct dielectric responses at different frequencies, multiband designs are highly useful, enabling broader absorption and improved performance across a wide frequency range. Therefore, the development of multiband absorbers is essential for enhancing the effectiveness of various sensing applications [16], [17]. Recent advances in THz metasurface technologies have demonstrated tunable and reconfigurable functionalities, including frequency multiplexing, amplitude modulation, switchable polarization conversion, and programmable scattering control, utilizing active materials such as graphene and vanadium dioxide (VO_2) [18]–[20].

In biomedical diagnostics, one of the major challenges is the early and accurate identification of diseases such as cancer and malaria. Cancerous tissues exhibit changes in cellular shape and biochemical composition, leading to distinctive dielectric properties at THz frequencies [21]. Malaria infections also alter red blood cells, altering hemoglobin levels and membrane properties, which changes their behavior in an electromagnetic field [22]. THz metamaterial absorbers exhibit remarkable capabilities for confining fields and generating stronger, localized electric fields at resonance. This greatly increases the interaction of THz waves with biological samples near the resonator surface. The improved light-matter interaction makes it easier to detect small changes in refractive index and absorption coefficients associated with disease. For biomedical sensing applications, designing metamaterial sensors requires high sensitivity (S), a high Q- factor, a low full-width at half-maximum (FWHM), and a high figure of merit (FOM). The metamaterial sensor has been investigated in both single-band [23], [24], [25] and multiband configurations [13], [26], [27], [28], [29], [30]. Multiband designs have gained increasing interest because of their ability to provide multiple sensing channels within a compact footprint. In [13], a triple-band THz biosensor for non-melanoma skin cancer detection is presented, achieving a highest Q-factor of 33.97 and sensitivity of 3.337 THz/RIU. A multiband metasurface sensor was introduced in [26] for detecting malaria and brain cancer, achieving a maximum Q-factor of 18.33 and a sensitivity of 1.43 THz/RIU. Consequently, a triple-band metamaterial sensor demonstrated better sensing performance for six cancer types [27]. Its highest Q-factor was 23.2, and its sensitivity reached 4.8 THz/RIU at one of its resonant modes. Similarly, Pahadsingh et al. [28] presented a triple-band sensor for breast and blood cancer detection, reporting a maximum Q-factor of 23 and a sensitivity of 1.7183 THz/RIU. In [29], a triple-band absorber developed for diagnosing blood cancer had a higher Q-factor of 34.74 and a sensitivity of 2.54 THz/RIU. The six-band metamaterial sensor described in [30] had a maximum Q-factor of 17.45 and a sensitivity of 3.7 THz/RIU. These multiband sensors are showing promising results, but their Q factors and sensitivities remain limited. This implies they need further optimization to improve field confinement and refractive index resolution.

The key contributions of this work can be summarized as follows:

1. Design and analysis of a polarization-insensitive MSA operating in the 1–6 THz frequency range.
2. Achieving six near-unity absorption resonances (>98%) at 1.80, 2.89, 4.65, 4.84, 5.12, and 5.84 THz, enabling multiband sensing capability.
3. Achieving narrow resonance linewidths and high Q-factors of up to 177, providing excellent spectral selectivity and frequency discrimination.
4. Evaluation of refractive-index sensing performance for biological analytes, achieving a maximum sensitivity of 2.92 THz/RIU for cancer-related samples and 8 THz/RIU for malaria-infected blood (Ring Stage), demonstrating its potential for high-resolution THz biosensing applications.

This work presents a simple multiband metasurface absorber (MSA) utilizing a dual split-ring resonator (SRR) configuration for the terahertz (THz) biomedical sensing applications. Unlike conventional single-resonator THz absorbers, the proposed dual-SRR configuration supports multiple coupled resonant modes within a single unit cell. The electromagnetic coupling between the concentric SRRs and the metallic ground plane enhances resonance confinement, enabling the simultaneous realization of multiband operation, high Q-factors, and improved refractive-index sensing performance. The unit cell consists of a compact MDM structure that provides near-unity absorption, angular stability, and compatibility with standard microfabrication techniques. The dual-SRR geometry significantly enhances electromagnetic field confinement at resonance, strengthening light-matter interactions and increasing sensitivity to refractive-index variations in the surrounding medium. The proposed MSA exhibits six absorption peaks exceeding 98%, with a maximum Q-factor of 177, indicating strong resonance confinement. It shows sensitivities of 2.92 THz/refractive index unit (n) for cancer-related samples and 8 THz/RIU for malaria-related samples, both of which are relevant to biological applications. These results compare favorably with other multiband terahertz (THz) absorbers.

2. DESIGN AND SIMULATION

Figure 1 shows the optimized geometry of the proposed MSA. The proposed absorber consists of three layers: gold resonators, a polyimide dielectric substrate, and a full gold ground plane, as depicted in Fig. 1(a). Two split-ring resonators (SRRs) with a thickness of t_m=0.3 µm are hosted on a polyimide dielectric substrate (ε_r = 3.5, δ = 0.0027, and thickness of t_s=2.8 µm), followed by a full ground plane with a thickness of 0.3 µm. The metallic top and bottom layers are made of gold with a conductivity of 4.561×10^7 S/m. The optimized dimensions of the proposed unit cell are P= 80 µm, R_1= 35 µm, R_3= 23 µm, W_1= 7 µm, W_2= 7 µm, and g= 6 µm. The dimensions are set to achieve multiband absorption characteristics. To analyze the electromagnetic response of the MS absorber, a full-wave simulation of the proposed design was conducted using CST Microwave Studio's frequency-domain solver. The periodic boundaries (unit cell boundary) have been applied across the x-y axes and open axes across the z-axis. Floquet ports with TE and TM modes were used for excitation along the z-axis. In addition, the simulation was conducted in the 1-6 THz range with a tetrahedral mesh of 112,568 elements, achieving a resolution of about 0.0005 THz. Subsequently, the proposed MSA was analyzed to assess its potential as a biosensor, with an analyte layer of thickness t_a = 1 µm placed above the top metallic resonators, as depicted in Fig. 1(d).

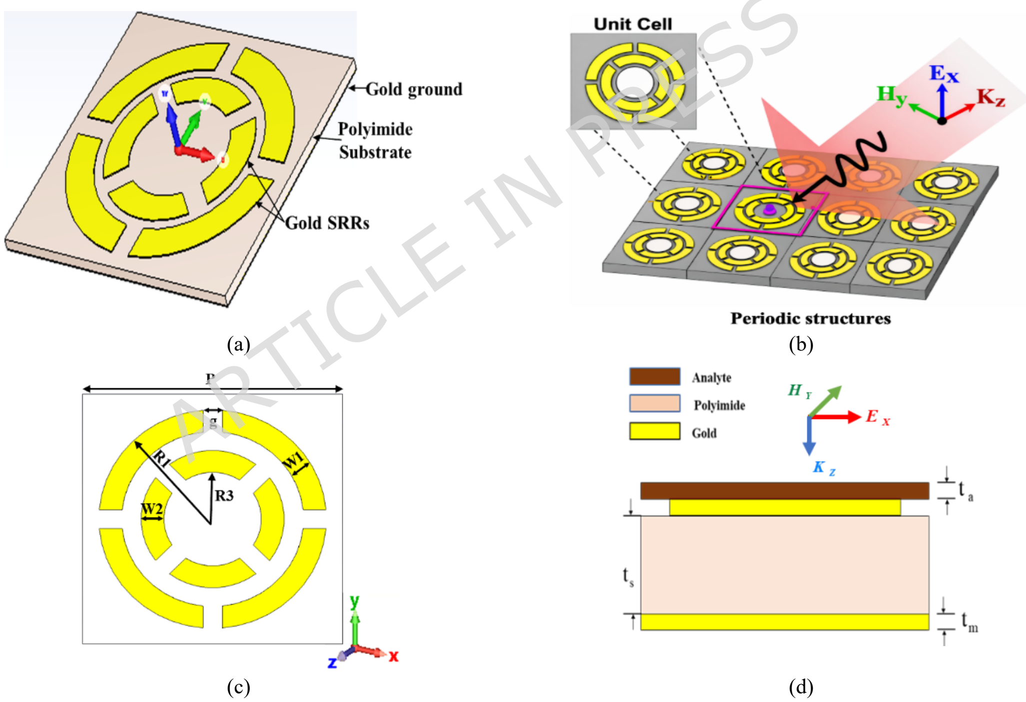

Fig.1. Geometry of the proposed MS absorber (a) perspective view, (b) periodic structures, (c)top view with dimensions, and (d) absorber with analyte

The proposed absorber can be manufactured using microfabrication techniques [31], [32] or electron-beam evaporation technology [33]. The fabrication process is well-suited for THz metasurfaces with micron-scale features. It involves depositing a gold ground plane, spin-coating a polyimide dielectric spacer, and patterning the top resonator using photolithography and lift-off processes. The smallest critical feature is the split gap, which is within the resolution of conventional lithographic techniques. Although fabrication imperfections, such as dimensional deviations, surface roughness, and layer-thickness variations, may introduce slight resonance shifts, the parametric study indicates that the key geometrical parameters primarily govern the resonance characteristics. Experimental characterization of the fabricated absorber can be performed using a Fourier-transform infrared (FTIR) spectrometer [34]. The measured transmittance T(ω) and reflectance R(ω) can then be used to calculate the experimental absorption A(ω).

3. RESULTS AND DISCUSSION

3.1 Evaluation of the Design

Figure 2 illustrates the evaluation steps of the proposed metasurface absorber and the corresponding absorptivity at each stage. The numerical analysis of the three design stages of the proposed absorber has been conducted, as shown in Fig. 2(a). The absorptivity rate can be determined as follows

$$A(\omega) = 1 - R(\omega) - T(\omega) \tag{1}$$

where $R(\omega) = |S_{11}|^2$ and $T(\omega) = |S_{21}|^2$. As the bottom layer is a full metallic layer, $T(\omega) = |S_{21}|^2 = 0$. Near-unity absorption can be achieved by reducing reflectance, thereby allowing most of the incident wave to be absorbed and resulting in high electrical and magnetic losses. These losses are linked to the imaginary parts of permittivity and permeability. To assess the performance of the proposed structure, three different simulations were performed, and the results are shown in Fig. 2(b).

In the first stage, the initial structure consists of a circular resonator hosted on a polyimide substrate, backed by a metallic layer. This configuration exhibits four absorption peaks exceeding 93%, 92%, 94%, and 78% at 1.25 THz, 4.63 THz, 4.85 THz, and 5.73 THz, respectively. In the second stage, an extra circular element is integrated into the resonator. This design produces five unique absorption peaks, recorded at 91%, 84%, 91%, 90%, and 99% at frequencies of 1.05 THz, 1.84 THz, 4.68 THz, 4.84 THz, and 5.77 THz, respectively, as depicted in Fig 2(b). In the final stage, four gaps are introduced to each resonator, resulting in a split-ring resonator (SRR) configuration. This design has six strong absorption peaks exceeding 98% at 1.80 THz, 2.89 THz, 4.65 THz, 4.84 THz, 5.12 THz, and 5.84 THz, as depicted in Fig. 2(b).

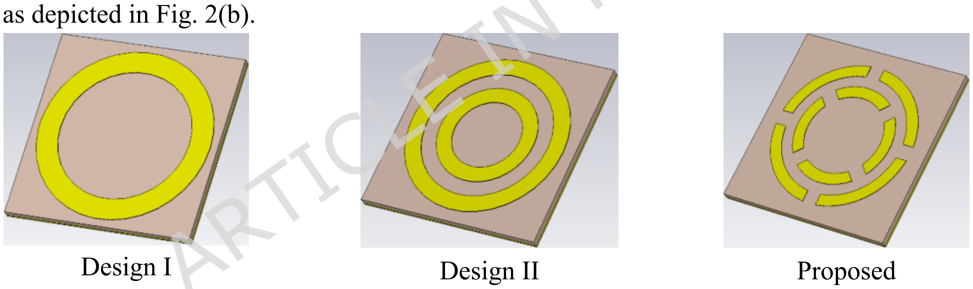

(a)

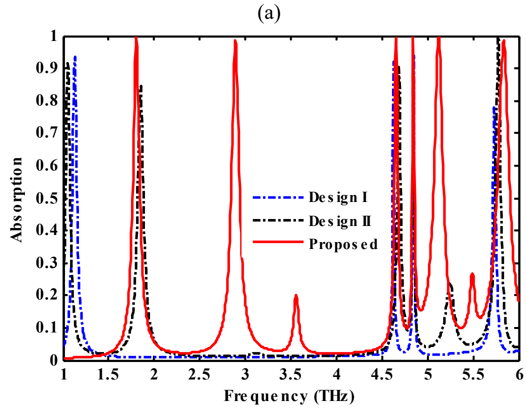

(b)

Fig. 2. (a) Sequential evaluation steps of the proposed MS absorber; (b) absorptivity corresponding to each evaluation step.

Figure 3 illustrates the absorption, reflection, and transmission coefficients of the proposed MSA. At normal incidence, near-unity absorption peaks of 99.9%, 99%, 99.7%, 99.8%, 99.8%, and 98.5% are observed at frequencies of 1.80 THz, 2.89 THz, 4.65 THz, 4.84 THz, 5.12 THz, and 5.84 THz, respectively, all accompanied by low reflection coefficients. Additionally, the transmission remains nearly zero because of a full ground plane.

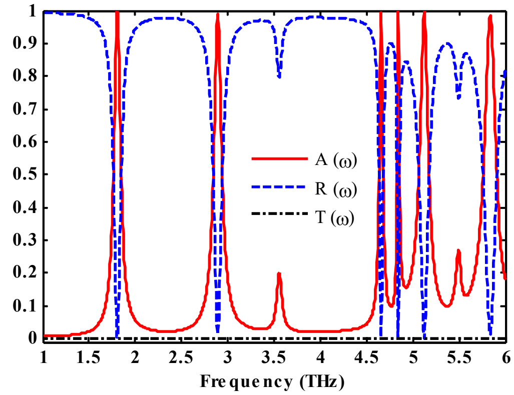

Fig. 3. Absorption, reflection, and transmission coefficients for the proposed absorber under normal incidence

The proposed metasurface structure is further examined to evaluate its ability to capture power under both TE and TM polarizations, as shown in Fig. 4. The results indicate that the proposed structure exhibits uniform absorption properties across both polarizations due to its symmetrical design. This confirms the metasurface's polarization independence. As depicted in Fig. 4, near-unity absorption exceeding 98% is achieved at the resonance frequencies.

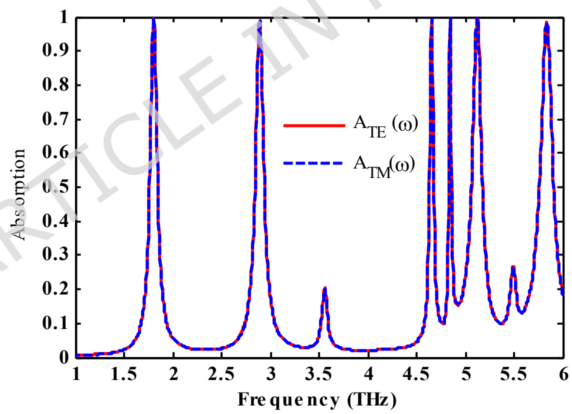

Fig. 4. Absorptivity under TE and TM polarization

Numerical simulations and analyses of the electric field (E-field) and magnetic field (H-field) distributions at all resonance frequencies are performed to achieve an extensive understanding of the electromagnetic function of the proposed MSA, as normal plane waves interact with the z-axis. Figure 5 shows the simulated E-field of the MSA at the operating frequencies of 1.80, 2.89, 4.65, 4.84, 5.12, and 5.84 THz. At 1.80 THz, the E-field is dominant along the outer resonator edges and split gaps, as illustrated in Fig. 5(a). The E-field is concentrated around these splits, demonstrating that the neighboring metallic segments are strongly capacitively coupled. This field confinement indicates that the resonance is primarily determined by the metal loop's inductance and the capacitance at the gaps. At the frequency of 2.89 THz, the E-field is dominant at the inner resonator, as depicted in Fig. 5(b). The results show that a higher-order mode with a stronger field has been created. This redistribution suggests improved capacitive coupling, making the inner area more sensitive to structural features. The E-field is evenly distributed across both the inner and outer resonators at 4.65 THz. The significant increase in the field at the resonator gaps indicates modal hybridization. This results in energy being absorbed and shared among the resonant components, producing a pronounced resonant response. At 4.84 THz, the E-field exhibits a more complex pattern, with significant localization in the resonator's gaps and arms, as depicted in Fig. 5(d). This observation demonstrates the excitation of a higher-order resonance mode, which increases the interaction between neighboring resonator segments. As illustrated in Fig. 5(e), the field strength keeps rising to 5.12 THz and spreads more evenly across the whole metasurface. The strong E-field amplification in both the resonators and the surrounding regions indicates that the resonance states are extremely close. This means energy is stored more efficiently and electromagnetic interactions are stronger. Finally, at the resonance of 5.84 THz, as shown in Fig. 5(f), the E-field demonstrates several localized hot spots evenly spaced around the resonator structure. The enhancement of the key field around the gaps and edges suggests that electromagnetic confinement is stronger.

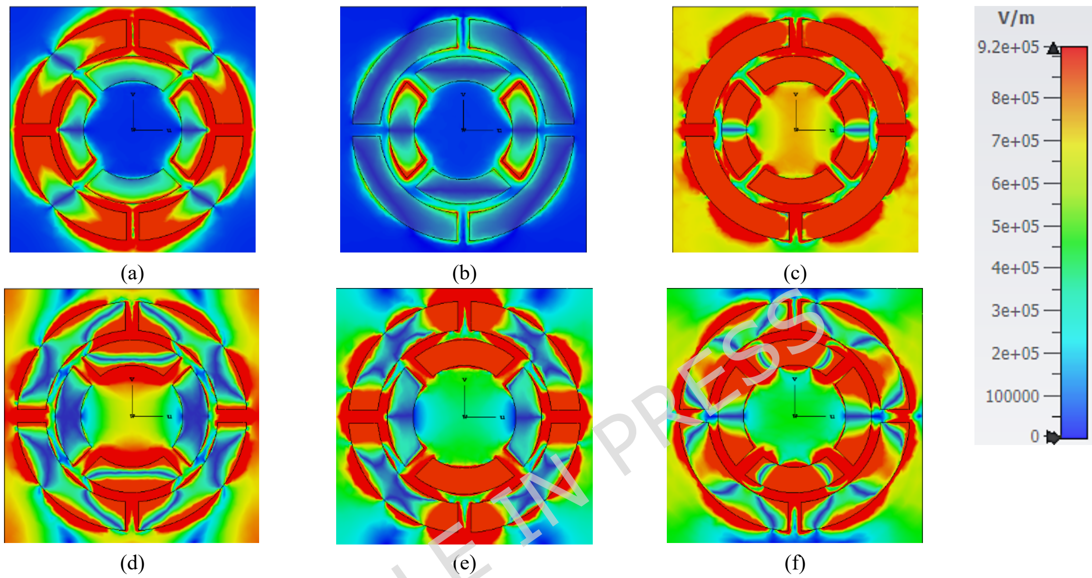

Fig. 5. E-field distributions: (a) 1.80 THz, (b) 2.89 THz, (c) 4.65 THz, (d) 4.84 THz, (e) 5.12 THz, and (f) 5.84 THz.

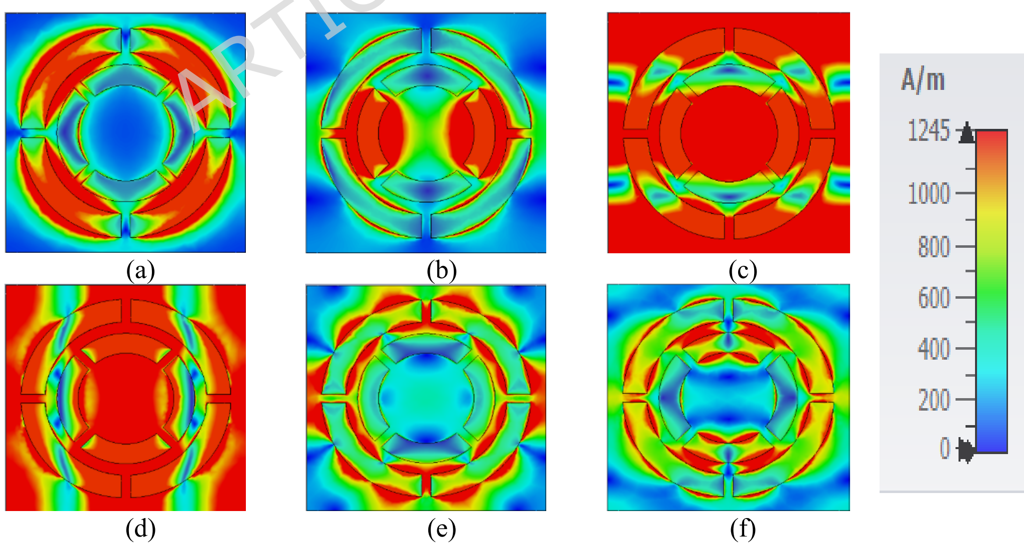

Fig. 6. H-field distributions: (a) 1.8 THz, (b) 2.89 THz, (c) 4.64 THz, (d) 4.84 THz, (e) 5.12 THz, and (f) 5.84 THz

Figure 6 illustrates the H-field distributions of the proposed MSA at its resonance frequencies. At 1.80 THz (Fig. 6(a)), the H-field is strongly confined within the dielectric spacer between the top resonator and the ground plane, indicating a magnetic dipole resonance driven by anti-parallel surface currents. At 2.89 THz (Fig. 6(b)), the field distribution shifts toward the inner resonator region, suggesting a higher-order magnetic mode with enhanced field localization. For the 4.65 THz resonance (Fig. 6(c)), the H-field spreads across both the inner and outer resonator gaps, confirming modal hybridization and strong inductive coupling. At 4.84 THz (Fig. 6(d)), a more complex pattern emerges, with multiple localized hot spots corresponding to a higher-order mixed mode. At the 5.12 THz resonance (Fig. 6(e)), the H-field concentrates in the inner split-ring gaps. In comparison, the 5.84 THz resonance (Fig. 6(f)) displays a distributed field pattern across the unit cell, characteristic of a higher-order standing wave.

Figure 7 shows the surface current distributions of the proposed absorber at six resonance frequencies. These distributions provide significant insight into the origins of the observable spectral characteristics and how the underlying resonant modes form. At 1.80 THz, the current density is predominantly concentrated along the outer resonator, as shown in Fig. 7(a), indicating a fundamental dipole-like resonance intrinsic to the overall antenna geometry. At 2.89 THz, the current density becomes more focused within the inner resonator, especially along the x-axis, as shown in Fig. 7(b). At 4.65 THz, however, the current density is spread over both the inner and outer resonators, as shown in Fig. 7(c). A distinct quadrupole-like pattern emerges at 4.84 THz, as shown in Fig. 7(d), which accounts for the sharp, high-Q Fano resonance resulting from the cancellation of far-field radiation. At 5.12 THz, the current is distributed across the outer resonator and the edges of the inner resonator, resulting in significant field enhancement, as depicted in Fig. 7(e). Finally, at 5.84 THz, the distribution shows shorter-wavelength oscillations along the metallic strips, indicative of propagating surface plasmon polaritons or higher-order harmonic resonances, as shown in Fig. 7(f). These distributions show that the structure's multi-band resonant behavior is caused by the outer-ring resonance, coupling between the inner resonator, and the field enhancement induced by the gap.

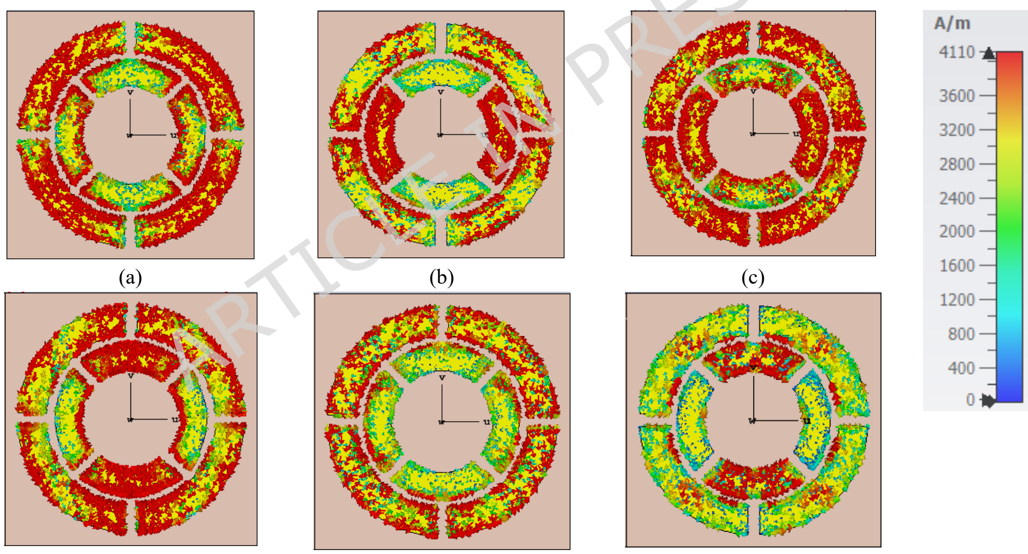

(a) (b) (c) (d) (e) (f)

Fig. 7. Current surface distributions: (a) 1.80 THz, (b) 2.89 THz, (c) 4.65 THz, (d) 4.84 THz, (e) 5.12 THz, and (f) 5.84 THz.

3.2 Absorption at different polarizations and incident angles

In real applications, designing an MS absorber with higher efficiency regardless of the incident polarization and angle is crucial. Thus, numerical simulation was carried out to evaluate the performance of the proposed absorber at different polarizations and incident angles. Figure 8 illustrates the absorption mechanism for the proposed absorber under different polarization angles. It is observed that the absorption peaks remain unchanged over a range of polarization angles from 0^o to 90^o, demonstrating that the metasurface structure provides polarization-insensitive absorption because of its geometric symmetry. Furthermore, the absorber's performance is computed at different incident angles from 0^o to 60^o in the step of 15^o, as shown in Fig. 9. It is observed that the first two resonances (1.80 THz and 2.89 THz) remain almost unaffected by angle, achieving a near-unity absorption across various incident angles, indicating strong, localized resonances with little dependence on the transverse wave vector. In contrast, the higher-frequency resonances at 4.65 THz, 4.84 THz, 5.12 THz, and 5.84 THz show moderate angular variation, with some broadening and decreased absorption at larger angles, typical of higher-order resonant modes.

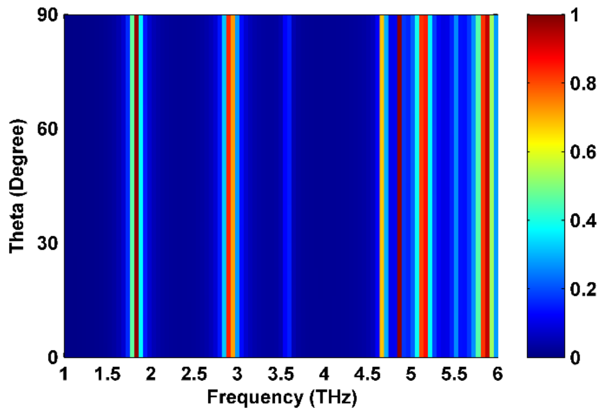

Fig. 8. Simulated absorptivity at various polarization angles.

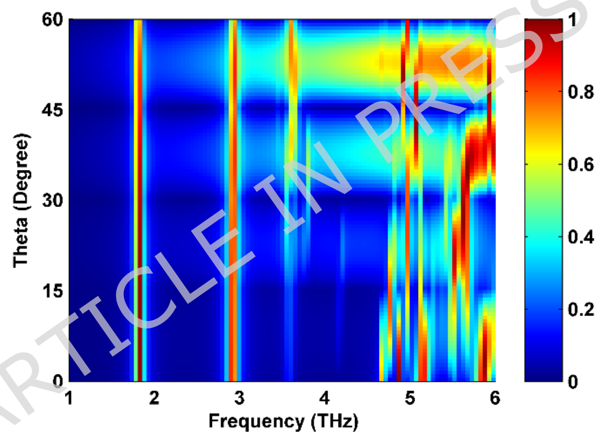

Fig. 9. Simulated absorptivity at various incident angles

3.3 Parametric Study

To improve the MSA absorption properties, a series of parametric sweep analyses has been conducted. The effect of the geometry parameters on the absorption performance, including the unit cell periodicity (P), substrate thickness (ts), the outer radius of the outer resonator (R1), the outer radius of the inner resonator (R3), the split's size (g), substrate loss tangent (tan δ), and gold conductivity (σ) has been investigated and analyzed as shown in Fig. 10. The effect of varying periodicity from 78 µm to 84 µm on the resonance frequencies is demonstrated in Fig. 10(a). As *P* increases, a slight shift toward higher frequencies is observed, while the absorption ratio remains constant. At $P = 80\ \mu m$, a near-unity absorption is observed across all resonance frequencies. Furthermore, as shown in Fig. 10(b), with a change in the substrate *ts*, the absorption peaks increase gradually, and the operating frequency changes significantly. The optimal absorption performance is achieved at $ts = 2.8\ \mu m$. On the other hand, changing *R1* results in a strong shift in *f1* and a slight shift in *f2*, while the dependence on the other frequencies *f3* to *f6* shows only a slight change in absorption strength, as shown in Fig. 10(c). In addition, as depicted in Fig. 10(d), a strong shift in *f2* is observed as the *R3* changes from 21 µm to 24 µm with an increment of 1 µm, while slight changes in the absorption strength are observed at *f1* and *f3* to *f6*. The optimal absorption performance exceeding 98% is achieved at $R3 = 23\mu m$. The effect of *g* on absorption performance is shown in Fig. 10(e). A strong shift in the operating frequencies from *f1* to *f6* is observed as the *g* value changes from 2 µm to 8 µm in 2 µm increments, accompanied by a corresponding change in absorption strength. Optimal performance is obtained with *g = 6 µm*. The impact of *(tan δ)* variation on the absorption ratio is shown in Fig. 10(e). It is observed that all six absorption peaks exceed 98%, and the frequency shifts are less than 0.01 THz, indicating robustness against typical polyimide losses. Similarly, the effect of varying *(σ)* is shown in Fig. 10(f). Even at the lowest conductivity, the absorption is near-unity (above 97%) at the resonance frequencies.

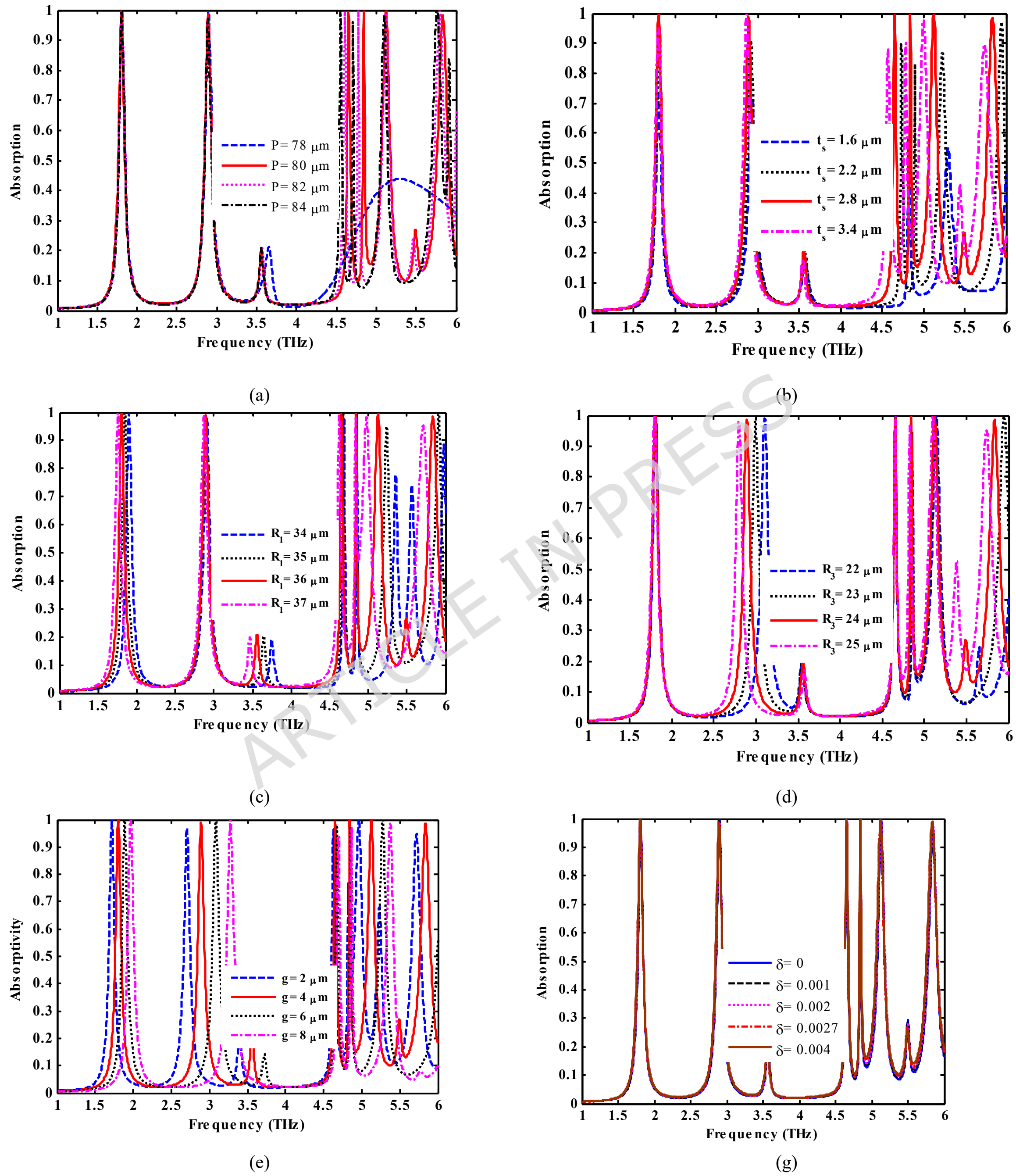

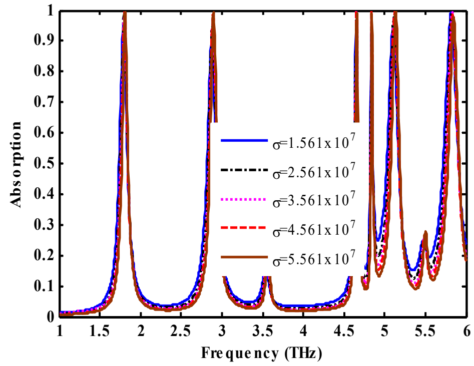

(g)

Fig. 10. Absorption performance as a function of the geometric parameters, (a) unit-cell periodicity, (b) substrate thickness (ts), (c) outer radius of the outer resonator (R1), (d) outer radius of the inner resonator (R3), (e) split size (g), (f) substrate loss tangent (δ), and (g) gold conductivity (σ).

3.4 Sensing Performance

The Quality factor (Q-factor), figure of merit (FOM), and refractive index sensitivity (S) are essential metrics for evaluating sensor performance in terahertz sensing applications. The Q-factor can be calculated as follows

$$Q = \frac{f_0}{FWHM} \tag{2}$$

where f_0 is the central frequency [35]. Table I shows the resonance characteristics of the proposed MSA, including resonance frequency, FWHM, and Q-factors. The high Q factor makes the proposed absorber suitable for sensor applications across different test media in the THz region. The Q-factor values were calculated using equation (2). The simulation was conducted in the 1-6 THz range with a tetrahedral mesh of 112,568 elements, achieving a resolution of about 0.0005 THz. This resolution is much smaller than the resonance linewidths, ensuring that the Q-factor values accurately reflect the resonance characteristics of the proposed absorber.

Table I. Resonance characteristics including resonance frequency, FWHM, and Q-Factor

Resonance Frequency (THz)	**Absorption rate (%)**	**FWHM (THz)**	**Q-Factor**
1.80	99.9	0.08	21.3
2.89	99	0.10	29.40
4.65	99.8	0.04	105.52
4.84	99.7	0.03	178.05
5.12	99.8	0.12	43.82
5.84	98.5	0.15	38.70

3.4.1 Variation in t_a and its Sensing

To explore the application of the proposed absorber as a sensor, an analyte layer of thickness (t_a) is applied to the absorber's top surface, as illustrated in Fig. 1(d). The analyte thickness (t_a) is varied from 1 µm to 7 µm in 2 µm increments, and the analyte is assigned a refractive index (n) of 1.35. Figure 11 shows the absorption properties of the proposed MSA as a function of frequency across the analyte thicknesses. The resonance frequencies tend to decrease with increasing analyte thickness, especially for *f3* and *f6*. This is because the dielectric layer becomes thicker, increasing the effective refractive index. At the same time, the overall absorption amplitude decreases significantly.

These data demonstrate that the absorber maintains consistent absorption levels despite variations in analyte thickness. The resonance frequencies are highly sensitive to changes in the surrounding dielectric environment. For an analyte thickness of 1 µm, the absorption magnitude is about 99% at six resonance frequencies, indicating a strong light–matter interaction within the near-field region. Therefore, this thickness is taken as the representative sensing layer to estimate the intrinsic refractive-index sensitivity of the proposed structure [24], [36]. However, real biological samples may exhibit size and structural heterogeneity that could influence the experimental resonance response.

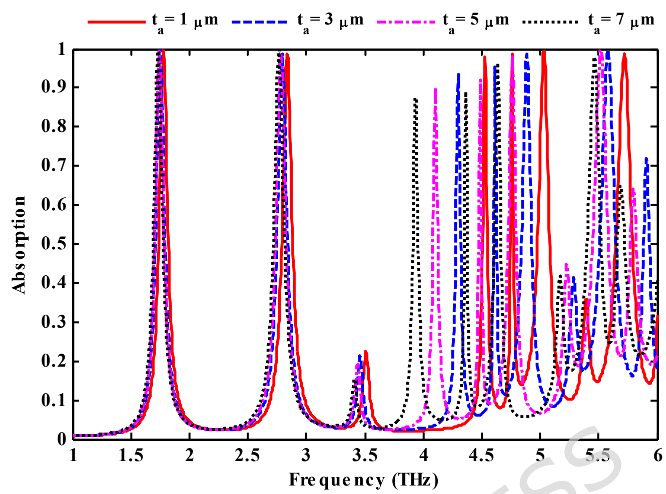

Fig. 11. Absorption versus resonance frequency for various analyte thicknesses (t_a)

To evaluate the sensing capabilities of the proposed MS sensor, the refractive index (n) of the 1 µm-thick analyte layer was varied from 1.2 to 2. Figure 12 illustrates the absorption response as the refractive index (n) varies. It is observed that as the refractive index (n) increases, the resonance frequencies shift to lower values, indicating a stronger interaction between the metasurface and its surrounding environment. At the same time, the absorption magnitude remains nearly constant over the investigated range, with an absorption efficiency of 93%, even as the refractive index changes. Table II presents a comprehensive study of the sensor's resonant properties as the refractive index increases by 0.2 over the specified range. Six distinct resonant modes are observed, indicating that the proposed design can sense in multiple ways. Additionally, Table II provides a comprehensive overview of the resonance frequencies, FWHM, sensitivity (S), and Q-factor associated with each refractive index value investigated. The sensitivity is determined as follows

$$S = \frac{\Delta f_0}{\Delta n} \tag{3}$$

where $\Delta f_0 = f_2 - f_1$ indicates the shift in resonance frequency, and $\Delta n = n_2 - n_1$ signifies the change in refractive index, with sensitivity expressed in units of THz/RIU. When the refractive index increases, all six resonance frequencies change significantly. This shows that the absorber's behavior depends on the refractive index. The sensitivity values depend on the mode and refractive index; they typically range from 0.05 to 0.5 THz/RIU. In addition, peaks *f5* and *f6* are more sensitive than the other peaks. For instance, at a refractive index of 1.2, peak *f3* has a high sensitivity of 0.5 THz/RIU. Furthermore, peak *f6* is quite sensitive to a wide range of refractive indices. Most resonance peaks have low FWHM values, especially peaks *f3* and *f4*, which immediately enhance the Q-factors. At the peak frequency *f4*, the highest Q-factor was reached for lower refractive indices. The maximum Q-factor was attained for lower refractive indices at the peak frequency *f4*. At a refractive index of n = 1.2, it rises to 183. As the refractive index increases, the Q-factor slowly decreases. However, the values remain high enough to ensure that resonance sharpness and detection capabilities are reliable. This demonstrates the proposed sensor's features as a refractive index sensor. It would be beneficial for biological sensing, environmental monitoring, and optical detection systems, where accurate detection of small refractive index changes is important.

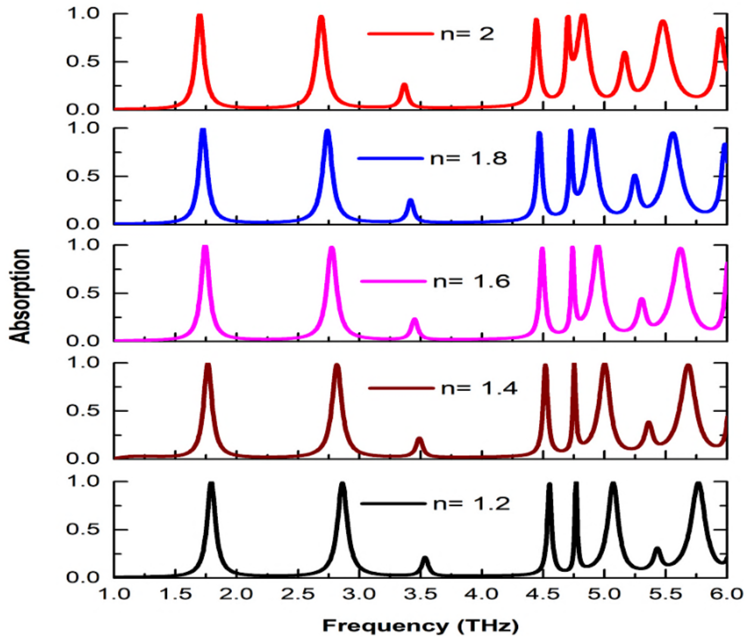

Fig. 12. Absorption response as the refractive index varies from 1 to 2

Table II. Performance evaluation of the proposed sensor for various refractive indices (n)

Peaks (THz)	*f1*	*f2*	*f3*	*f4*	*f5*	*f6*
n=1.2						
f_r	1.79	2.86	4.55	4.77	5.07	5.77
FWHM (THz)	0.083	0.096	0.043	0.026	0.107	0.142
S (THz/RIU)	0.05	0.15	0.5	0.35	0.25	0.35
Q-Factor	21.59	29.75	106.71	183.15	47.57	40.42
n=1.4						
f_r	1.76	2.82	4.52	4.75	5	5.68
FWHM (THz)	0.082	0.096	0.047	0.03	0.111	0.150
S (THz/RIU)	0.15	0.2	0.15	0.1	0.35	0.45
Q-Factor	21.37	29.10	97.75	161.21	45.35	37.83
n=1.6						
f_r	1.74	2.78	4.49	4.74	4.95	5.62
FWHM (THz)	0.082	0.096	0.049	0.034	0.113	0.154
S (THz/RIU)	0.1	0.2	0.15	0.05	0.25	0.3
Q-Factor	21.35	28.83	91.10	142	43.69	36.44
n=1.8						
f_r	1.73	2.74	4.47	4.72	4.90	5.56
FWHM (THz)	0.081	0.094	0.053	0.039	0.117	0.158
S (THz/RIU)	0.05	0.2	0.1	0.1	0.25	0.3
Q-Factor	21.36	29.38	84.46	121.23	41.8	35.13
n=2						
f_r	1.70	2.69	4.44	4.70	4.83	5.48
FWHM (THz)	0.080	0.095	0.060	0.205	0.203	0.167
S (THz/RIU)	0.15	0.25	0.15	0.1	0.35	0.4

Q-Factor	21.16	28.35	75.07	23.13	23.9	33.22

The relationship between the resonance frequencies (*f1-f6)* and the refractive index (n) is illustrated in Fig. 13, showing a decrease in the frequencies as the refractive index (n) increases. Additionally, there is a linear correlation between resonance frequencies and the refractive index (n) across all resonance bands. The numerical fits for these linear relationships are derived from the following equations

$$f1 = 1.912 - 0.105\times n \quad (3)$$

$$f2 = 3.114 - 0.210\times n \quad (4)$$

$$f3 = 4.710 - 0.135\times n \quad (5)$$

$$f4 = 4.872 - 0.085\times n \quad (6)$$

$$f5 = 5.414 - 0.290\times n \quad (7)$$

$$f6 = 6.182 - 0.350\times n \quad (8)$$

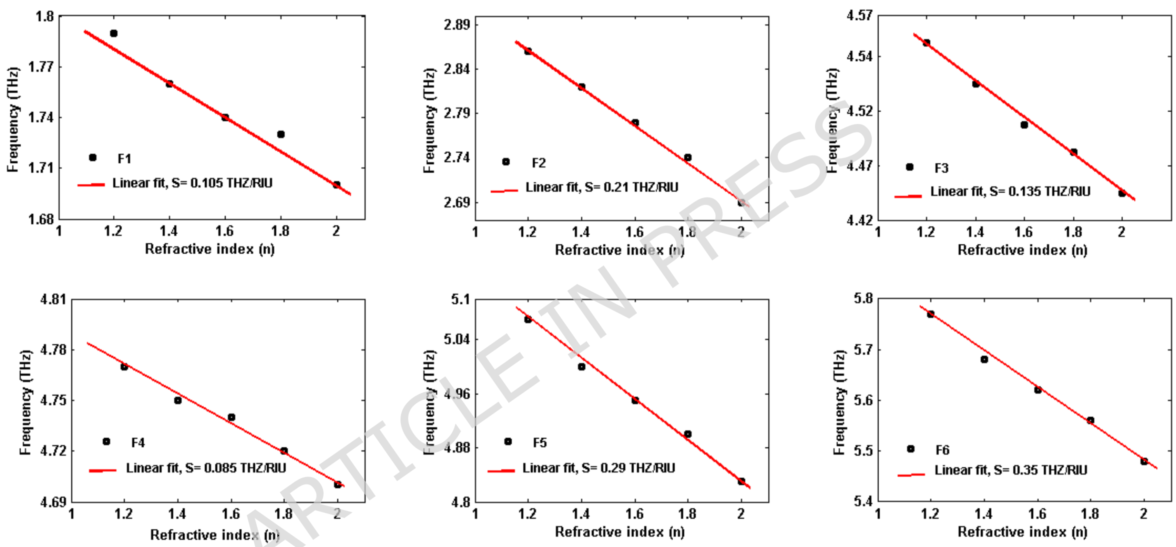

Fig. 13. Distribution of the resonance frequencies (*f1–f6*) with linear fit

3.5 Applications for Cancer Cell Detection

The differences in refractive index resulting from biochemical changes in cancer cells can be effectively leveraged for biomedical identification. Cancer cells typically have a higher protein concentration than healthy cells [37], [38], leading to higher refractive indices and measurable dielectric variations. These variations enable discrimination between healthy and cancerous samples via resonance-based sensing. Table III summarizes the resonance frequencies, sensitivities, and Q-factors of the proposed metasurface for normal and cancer-related biological samples. The refractive indices of healthy and cancerous human blood are 1.35 and 1.39, respectively [39]. As shown in Table III, the healthy blood exhibits a maximum Q-factor of 172.67 at *f4* and a minimum Q-factor of 21.61 at *f1*. For cancerous blood, the Q-factor drops to 150.04 at *f4* and 95.50 at *f3*, indicating measurable resonance shifts due to refractive-index (n) variation. Similarly, the refractive indices (n) of healthy basal skin and basal skin cancer are 1.36 and 1.38, respectively [24]. The corresponding maximum Q-factors of healthy and cancerous basal skin are 172.12 and 152.11, respectively, at *f4,* and the minimum ones are observed at *f1* (~21.6). The highest Q-factors for healthy and cancerous HeLa cells (n = 1.368 and 1.392, respectively [40]) are 171.65 and 150.66 at *f4*, respectively, and the lowest values are at *f1* (~21.6). Resonance shifts indicate sensitivity to changes in refractive index (n). The highest Q-factors for healthy and cancerous MCF-7 cells (n = 1.36 and 1.401, respectively [27]) are 172.12 and 151.40 at *f4*. These results demonstrate consistent resonance variations with refractive-index changes, confirming the suitability of the proposed metasurface for refractive index-based biosensing.

The sensitivity is calculated using Eq. (3). To illustrate this calculation explicitly for human blood analysis, healthy blood with a refractive index of $n_{healthy} = 1.35$ is considered, where the resonance frequency of peak *f1* was extracted as $f_{healthy} = 1.78$ THz. For cancerous blood with a reactive index of $n_{cancer} = 1.39$, the frequency shifted to $f_{cancer} = 1.75$ THz. The resulting frequency shift is therefore $\Delta f = \left| f_{cancer} - f_{health} \right| = 30$ GHz. The corresponding change in refractive index is $\Delta n = \left| n_{cancer} - n_{health} \right| = 0.04$ RIU. Substituting these values into the sensitivity formula in Eq. (3), the sensitivity is obtained as $S = \Delta f / \Delta n = 30 \text{ GHz} / 0.04 \text{ RIU} = 750 \text{ GHz/RIU}$. The same procedure was applied to all resonance peaks and across the entire refractive index (n) range under investigation. The achieved sensitivity is sufficient to resolve refractive index differences as small as 0.01 RIU, well below the reported optical contrast between healthy and cancerous cells, highlighting its potential for label-free biomedical diagnostics.

Table III: Performance Evaluation of the Proposed Metasurface Sensor in Various Cancer Cell Types

Peaks		***f1***	***f2***	***f3***	***f4***	***f5***	***f6***
State		**Human blood**					
f_r	Healthy	1.78	2.84	4.53	4.76	5.03	5.72
	Cancer	1.75	2.80	4.52	4.75	4.98	5.65
Δf (GHz)		30	40	10	10	50	50
FWHM (THz)	Healthy	0.083	0.095	0.045	0.028	0.107	0.144
	Cancer	0.083	0.097	0.047	0.032	0.115	0.157
Q-factor	Healthy	21.61	29.82	101.96	172.67	47.04	39.69
	Cancer	21.10	29.05	95.50	150.04	43.35	36
S (GHz)		750	1000	250	250	1250	1750
State		**Basal Skin**					
f_r	Healthy	1.78	2.84	4.53	4.76	5.03	5.72
	Cancer	1.76	2.81	4.52	4.75	4.99	5.67
Δf (GHz)		20	30	10	10	40	50
FWHM (THz)	Healthy	0.082	0.095	0.044	0.027	0.107	0.145
	Cancer	0.083	0.097	0.047	0.031	0.115	0.157
Q-factor	Healthy	21.62	29.82	101.61	172.12	46.98	39.44
	Cancer	21.12	29.10	95.71	152.11	43.49	36
S (GHz)		1000	1500	500	500	2000	2500
State		**Cervical (Hela)**					
f_r	Healthy	1.78	2.83	4.52	4.76	5.03	5.72
	Cancer	1.75	2.80	4.52	4.75	4.98	5.65
Δf (GHz)		30	30	0	10	50	70
FWHM (THz)	Healthy	0.082	0.095	0.044	0.028	0.107	0.145
	Cancer	0.083	0.096	0.048	0.031	0.114	0.156
Q-factor	Healthy	21.62	29.83	101.41	171.65	46.95	39.56
	Cancer	21.13	29.03	94.78	150.66	43.46	36.06
S (GHz)		1250	1250	0	420	2080	2920
State		**MCF-7**					
f_r	Healthy	1.78	2.84	4.53	4.76	5.03	5.72
	Cancer	1.75	2.80	4.51	4.75	4.98	5.65
Δf (GHz)		30	40	20	10	50	70

FWHM (THz)	Healthy	0.082	0.095	0.044	0.027	0.107	0.145
	Cancer	0.083	0.096	0.048	0.032	0.115	0.158
Q-factor	Healthy	21.62	29.82	101.61	172.12	46.98	39.44
	Cancer	21.10	28.93	94.32	151.40	43.29	35.90
S (GHz)		730	980	940	240	1220	1710

3.6 Malaria Detection

The proposed MSA is designed to detect variations in the analyte's refractive index (n), making it suitable for diagnosing malaria. This is significant because the refractive index of human red blood cells (RBCs) varies with different stages of malaria infection. Table IV presents the resonance characteristics of the proposed absorber for healthy RBCs (n = 1.399) and malaria-infected blood at different stages: schizont (n = 1.373), trophozoite (n = 1.383), and ring stage (n = 1.395) [41]. The Q-factor and sensitivity values are calculated using equations (2) and (3), respectively. For healthy RBCs, a high Q-factor of 160.94 at *f4* is observed, indicating strong field confinement. The Q-factor rises to 163.5 at *f4* during the schizont stage, and the high sensitivity of 0.385 THz/RIU is reached at *f6*. The Q-factor reaches 150.85 at *f4* in the trophozoite stage, while the highest sensitivity is 1.875 THz/RIU at *f6*. In the ring stage, the Q-factor remains high at about 150 at *f4*, and the highest sensitivity remains at *f6*, where it is 8 THz/RIU.

Table IV: Evaluation of the proposed biosensor's performance across various stages of malaria diagnosis

Peaks	***f1***	***f2***	***f3***	***f4***	***f5***	***f6***
Healthy RBC (n=1.399)						
***f_r* (THz)**	1.764	2.816	4.519	4.753	5.003	5.683
Q-Factor	21.39	29.31	97.76	160.94	45.34	37.76
Infected Blood – Schizont Stage (n=1.373)						
***f_r* (THz)**	1.766	2.822	4.522	4.755	5.006	5.693
Δf (GHz)	2	6	3	2	3	10
S (THZ/RIU)	0.077	0.231	0.115	0.077	0.115	0.385
Q-Factor	21.31	29.3	98.36	163.5	45.23	37.76
Infected Blood -Trophozoite Stage (n=1.383)						
***f_r* (THz)**	1.754	2.8	4.517	4.749	4.981	5.653
Δf (GHz)	10	16	2	4	22	30
S (THZ/RIU)	0.625	1	0.125	0.25	1.375	1.875
Q-Factor	21.09	29.04	94.83	150.85	43.39	35.76
Infected Blood -Ring Stage (n=1.395)						
***f_r* (THz)**	1.753	2.797	4.515	4.749	4.979	5.651
Δf (GHz)	11	19	4	4	24	32
S (THZ/RIU)	2.75	4.75	1	1	6	8
Q-Factor	21.08	29.05	94.61	149.95	43.44	35.98

4. Comparison Performance with Published Works

Unlike previously reported multiband absorbers, the proposed design achieves six distinct absorption bands with a simple dual-split-ring resonator structure on a single polyimide substrate. Additionally, the simultaneous achievement of six highly confined, polarization-insensitive resonances overcomes the typical trade-off between the number of bands and resonance quality observed in prior works. Table V provides a comprehensive comparison with other published THz metamaterial absorbers, highlighting the unique properties of the proposed design. The proposed absorber exhibits six resonances spanning 1–6 THz, suitable for multiband sensing. At all resonant frequencies, near-unity absorption (~99%) is achieved. The narrow FWHM values indicate high spectral selectivity, and Q factors up to 177 are much larger than those reported in many previous studies. The narrow linewidths and high Q-factors improve frequency discrimination, spectral resolution, and sensing performance. Furthermore, a sensitivity peak at 8 THz is observed. Despite idealized simulations, low-loss materials and high Q-factor (177) ensure robustness against material losses. The sensor's 0.01 RIU resolution is well below biological contrast ($\Delta n \approx 0.02–0.04$ RIU) [24], [37]-[40], with environmental effects mitigated by thin layers, microfluidics, and lock-in detection. These features make the proposed metasurface a promising platform for high-resolution refractive-index sensing of biomedical analytes, including cancer- and malaria-related samples. To ensure a fair comparison, all performance values presented in Table V for the proposed work and referenced studies are obtained from numerical simulations.

Table V: Evaluation of the Proposed MS Sensor with Previously Published Works

Ref.	No. of bands	f_r (THz)	$A(\omega)$ %	FWHM (THz)	Q-factor	Peak S (THz/RIU) (Numerical)	n	Ta (μm)	FOM (RIU^{-1})	Application
[13]	3	0.495 0.796 0.97	99 90 99	0.041 0.038 0.029	23.3 21.1 33.97	3.337	1.38	4	116.85	Non-Melanoma Skin Cancer Diagnostics
[16]	3	1.675 3.504 5.694	99.18 99.14 99.94	0.109 0.206 0.370	15.37 17.01 15.39	1.636	NA	4	4.421	Cancer, Tumor, Virus, Malaria
[26]	3	0.5215 0.9873 1.5763	94.3 76.52 98.64	0.0340 0.0599 0.0798	15.33 16.48 19.75	1.43	1.395	4	17.54	Cancer and Malaria
[27]	3	2.474 4.678 8.717	99.9 99.9 99.8	0.18 0.274 0.376	13.7 17.0 23.2	4.571	NA	2	12.16	Cancer
[28]	3	0.7542 2.2333 3.2901	78 99.41 99.57	0.0419 0.0848 0.1562	17 24 23	0.6847	NA	5	4.383	Cancer
[29]	3	0.485 0.721 0.825	99.3 99.7 98.7	0.0218 0.0322 0.0258	24.86 24.86 34.74	2.54	1.39	5	98.6	Blood Cancer
[30]	6	3.003 7.4554 13.6447 20.3722 22.2858 25.2459	98 99.5 99 99.9 95.14 99.4	0.281 0.76 1.4 4.31 4.31 1.64	10.7 9.81 9.75 4.73 5.17 15.4	3.588	1.35	0.4	0.363	Cancer, Malaria, Tumor
[36]	3	1.095 2.865 4.065	99.6, 99.1 99.2	0.1 0.2 0.18	11.34 13.93 21.85	0.4763	1.39	1	2.57	Cancer
[42]	2	0.73 2.2	99.8 99.8	0.032 0.054	22.8 40.7	0.488	NA	10	19.52	Biomedical Sensing, Material Characterization
[43]	3	0.4267 0.9514 1.4365	99 97.8 98.8	0.0236 0.0557 0.1186	18.6 17.7 11	0.303	1.4869	10	4	Stomach cancer, Breast cancer, Skin cancer, Cervical cancer
[44]	2	1.994 2.7	100 88	-	12.24 8.9	0.8	1.38	8	2.65	Cancer
Pro.	**6**	**1.80 2.89 4.65 4.84 5.12 5.84**	**99.99 99 99.7 99.8 99.8 98.5**	**0.08 0.10 0.04 0.03 0.12 0.15**	**21.3 29.42 105.61 177 43.74 38.64**	**8**	**1.395**	**1**	**51**	**Blood Cancer, Human Basel Skin Cancer, Cervical (HeLa) Cancer, MCF-7 Cancer, and Malaria detection**

Note: All entries in this table are from numerical simulations (theoretical); no experimental results are included.

5. Conclusion

This study presents a multiband THz MSA for label-free, refractive-index-based biomedical sensing. The proposed structure consists of two split-ring resonators (SRRs) patterned on a polyimide substrate backed by a metallic ground plane, enabling strong electromagnetic field confinement and near-unity absorption. Six absorption peaks are observed at 1.80, 2.89, 4.65, 4.84, 5.12, and 5.84 THz, with absorptivity exceeding 98%. The absorber is polarization-insensitive and maintains high absorption across the investigated range of incident angles, confirming its structural symmetry and robustness. High Q-factors of 21.3, 29.42, 105.61, 177, 43.74, and 38.64, together with narrow FWHM values, provide excellent spectral selectivity and enhanced sensing resolution. The sensor achieves maximum sensitivities of 2.92 THz/RIU and 8 THz/RIU for refractive-index ranges representative of cancer- and malaria-related biological samples, respectively. High-Q resonances and narrow linewidths enable detection of subtle dielectric variations through resonance-frequency shifts. These findings are numerically supported, but real-sample biosensing requires experimental validation. Although current results stem from idealized numerical simulations, future work will focus on experimental validation in realistic biological settings, accounting for factors such as THz water absorption, sample heterogeneity, measurement noise, and fabrication tolerances through strategies including thin-sample or microfluidic measurement, spatial averaging, lock-in detection, and process control. Due to its structural simplicity and high sensitivity, the proposed metasurface absorber is a promising platform for advanced THz biosensing applications.

Funding: Not applicable

Acknowledgement

The authors gratefully acknowledge the funding and support provided by the Deanship of Scientific Research at Imam Mohammad Ibn Saud Islamic University (IMSIU) (grant number IMSIU-DDRSP2604).

Data Availability: The datasets used and/or analyzed during the current study are available from the corresponding author on reasonable request.

Author contributions

Conceptualization, Abdulrahman A.G. Amer, Yosef T. Aladadi, Ali Ahmed Salem, and Muhammad Zamir Mohyedin; methodology, Abdulrahman A.G. Amer., and Zaid Shamsan; software, Abdulrahman A.G. Amer, Zaid Shamsan, and Ali Ahmed Salem; formal analysis, Abdulrahman A.G. Amer, Aduwati Sali, and Shaiful Jahari Hashim; writing—original draft preparation, Abdulrahman A.G. Amer; supervision, Aduwati Sali, and Shaiful Jahari Hashim; writing—review and editing, Aduwati Sali, Zaid Shamsan, Ali Ahmed Salem, Yosef T. Aladadi, A.J.A. Al-Gubri; project administration, Aduwati Sali, and Shaiful Jahari Hashim; funding acquisition, Zaid Shamsan, Yosef T. Aladadi. All authors have read and agreed to the published version of the manuscript.

References

[1] M. Gezimati and G. Singh, "Terahertz Imaging and Sensing for Healthcare: Current Status and Future Perspectives," *IEEE Access*, vol. 11, pp. 18590–18619, 2023, doi: 10.1109/ACCESS.2023.3247196.
[2] W. Jiang *et al.*, "Terahertz Communications and Sensing for 6G and Beyond: A Comprehensive Review," *IEEE Commun. Surv. Tutorials*, vol. 26, no. 4, pp. 2326–2381, 2024, doi: 10.1109/COMST.2024.3385908.
[3] F. Capolino, *Theory and Phenomena of Metamaterials*.
[4] A. A. G. Amer, S. Z. Sapuan, N. B. Othman, A. A. Salem, A. J. A. Al-Gburi, and Z. Zakaria, "A Wide-Angle, Polarization-Insensitive, Wideband Metamaterial Absorber With Lumped Resistor Loading for ISM Band Applications," *IEEE Access*, vol. 12, no. March, pp. 42629–42641, 2024, doi: 10.1109/ACCESS.2023.3345659.
[5] A. A. G. Amer, S. Z. Sapuan, and N. Nasimuddin, "Efficient Metasurface Absorber for 2.4 GHz ISM-Band Applications," *2020 IEEE Student Conf. Res. Dev. SCOReD 2020*, no. September, pp. 471–474, 2020, doi: 10.1109/SCOReD50371.2020.9251029.
[6] A. Ahmed *et al.*, "Polarization-Insensitive, High-Efficiency Metasurface with Wide Reception Angle for Energy Harvesting Applications," *Sensors*, vol. 25, no. 2, pp. 1–17, Jan. 2025, doi: 10.3390/s25020429.

[7] K. Muthukrishnan and V. Narasimhan, "Multiband Terahertz Metamaterial Absorber Based on Multipolar Plasmonic Resonances," *Plasmonics*, vol. 16, no. 4, pp. 1049–1057, 2021, doi: 10.1007/s11468-020-01322-4.
[8] A. Ahmed, G. Amer, Z. A. Shamsan, and A. S. Algamili, "High-efficiency, polarization-independent broadband metasurface absorber with angular stability for ISM applications," *PLoS One*, vol. 21, no. 3, p. e0339385, Mar. 2026, doi: 10.1371/journal.pone.0339385.
[9] T. Alam, A. F. Almutairi, M. Samsuzzaman, M. Cho, and M. T. Islam, "Metamaterial array based meander line planar antenna for cube satellite communication," *Sci. Rep.*, vol. 11, no. 1, pp. 1–12, 2021, doi: 10.1038/s41598-021-93537-6.
[10] M. S. Khan, R. A. Shakoor, O. Fayyaz, and E. M. Ahmed, "A focused review on techniques for achieving cloaking effects with metamaterials," *Optik (Stuttg).*, vol. 297, no. November 2023, p. 171575, 2024, doi: 10.1016/j.ijleo.2023.171575.
[11] L. Dewangan, N. K. Mishra, and S. Ghosh, "Angularly Stable High-Q Factor Metamaterial Absorber for Biomedical Sensing Applications," *IEEE Sensors Lett.*, vol. 8, no. 8, pp. 1–4, 2024, doi: 10.1109/LSENS.2024.3414337.
[12] M. Shahnawaz, H. B. Baskey, and M. J. Akhtar, "An ultrathin broadband terahertz metasurface absorber with angular stability using graphene," *Diam. Relat. Mater.*, vol. 149, no. September, p. 111598, 2024, doi: 10.1016/j.diamond.2024.111598.
[13] M. N. Hamza *et al.*, "Designing a High-Sensitivity Microscale Triple-Band Biosensor Based on Terahertz MTMs to Provide a Perfect Absorber for Non-Melanoma Skin Cancer Diagnostic," *IEEE Photonics J.*, vol. 16, no. 2, pp. 1–13, 2024, doi: 10.1109/JPHOT.2024.3381649.
[14] N. I. Landy, S. Sajuyigbe, J. J. Mock, D. R. Smith, and W. J. Padilla, "Perfect Metamaterial Absorber," *Phys. Rev. Lett.*, vol. 100, no. 20, p. 207402, May 2008, doi: 10.1103/PhysRevLett.100.207402.
[15] H. Tao, N. I. Landy, C. M. Bingham, X. Zhang, R. D. Averitt, and W. J. Padilla, "A metamaterial absorber for the terahertz regime: design, fabrication and characterization," *Opt. Express*, vol. 16, no. 10, p. 7181, May 2008, doi: 10.1364/oe.16.007181.
[16] P. Binda, R. Kumar Singh, and S. Bhattacharyya, "An Ultraminiaturized Multiband Metasurface Absorber Toward Multifold Sensing Applications in Healthcare," *IEEE Trans. Plasma Sci.*, vol. 53, no. 7, pp. 1711–1721, 2025, doi: 10.1109/TPS.2025.3578731.
[17] J. Bai *et al.*, "An ultra-thin multiband terahertz metamaterial absorber and sensing applications," *Opt. Quantum Electron.*, vol. 53, no. 9, pp. 1–9, 2021, doi: 10.1007/s11082-021-03180-8.
[18] H. Mistri, A. R. Sardar, and A. Ghosh, "Dynamically reconfigurable graphene–vanadium dioxide metasurface with switchable polarization conversion, multiband absorption, and programmable scattering control," *Phys. Chem. Chem. Phys.*, vol. 28, no. 12, pp. 7570–7586, 2026.
[19] H. Mistri, A. Ghosh, and A. R. Sardar, "Graphene Metasurface-based Dual-Channel Frequency Multiplexed Binary Amplitude Shift Keying Modulator for Terahertz Applications," *Phys. status solidi*, vol. 263, no. 4, p. e70196, 2026.
[20] H. Mistri, A. Ghosh, and A. R. Sardar, "A tunable multifunctional multimodal graphene-vanadium dioxide metasurface enabling fabry-perot transmission, reflective polarization conversion, and multiband absorption," *Diam. Relat. Mater.*, vol. 163, p. 113431, 2026.
[21] Y. Peng, C. Shi, X. Wu, Y. Zhu, and S. Zhuang, "Terahertz Imaging and Spectroscopy in Cancer Diagnostics: A Technical Review," *BME Frontiers*, vol. 2020. American Association for the Advancement of Science, p. 2547609, Jan. 01, 2020. doi: 10.34133/2020/2547609.
[22] M. A. Agnero *et al.*, "Malaria-infected red blood cell analysis through optical and biochemical parameters using the transport of intensity equation and the microscope's optical properties," *Sensors (Switzerland)*, vol. 19, no. 14, p. 3045, Jul. 2019, doi: 10.3390/s19143045.
[23] H. V. Du John *et al.*, "Design and Simulation of SRR-Based Tungsten Metamaterial Absorber for Biomedical Sensing Applications," *Plasmonics*, vol. 18, no. 5, pp. 1903–1912, 2023, doi: 10.1007/s11468-023-01910-0.
[24] M. Y. Azab, M. F. O. Hameed, A. M. Nasr, and S. S. A. Obayya, "Highly Sensitive Metamaterial Biosensor for Cancer Early Detection," *IEEE Sens. J.*, vol. 21, no. 6, pp. 7748–7755, 2021, doi: 10.1109/JSEN.2021.3051075.
[25] M. M. E. Tammam, M. F. O. Hameed, E. M. A. Elkaramany, T. A. Ali, and S. S. A. Obayya, "Versatile Terahertz Metamaterial Sensor for Biomedical Applications," *Plasmonics*, vol. 20, no. 5, pp. 2815–2828, 2025, doi: 10.1007/s11468-024-02401-6.
[26] T. Sheheryar, Y. Tian, B. Lv, and L. Gao, "Transforming medical diagnostics with metasurface terahertz biosensing technology: a label-free biosensor for detecting multiple diseases," *Opt. Quantum Electron.*, vol.

57, no. 5, 2025, doi: 10.1007/s11082-025-08225-w.
[27] R. K. Singh, P. Binda, and U. Dey, “Investigations on a Triple-Band Metasurface Absorber as THz-Biomedical Sensor,” *IEEE Trans. Plasma Sci.*, vol. 52, no. 7, pp. 3051–3060, 2024, doi: 10.1109/TPS.2024.3431929.
[28] Shruti, S. Pahadsingh, and B. Appasani, “Hexagonal Tiled Terahertz Metamaterial Absorber for Cancer Detection Incorporating Machine Learning,” *IEEE Sens. J.*, vol. 24, no. 10, pp. 16093–16101, 2024, doi: 10.1109/JSEN.2024.3384972.
[29] M. N. Hamza *et al.*, “A Very Compact Metamaterial-Based Triple-Band Sensor in Terahertz Spectrum as a Perfect Absorber for Human Blood Cancer Diagnostics,” *Plasmonics*, vol. 20, no. 2, pp. 1015–1028, 2025, doi: 10.1007/s11468-024-02291-8.
[30] V. Maurya and S. Singhal, “Ultrathin Multiband Polarization-Independent Terahertz Absorber as a Biosensor,” *IEEE Sens. J.*, vol. 23, no. 21, pp. 25919–25926, 2023, doi: 10.1109/JSEN.2023.3311018.
[31] K. B. S. Sri Nagini and D. S. Chandu, “Wideband and Tunable Reflective Cross-Polarization Conversion Metasurface for TeraHertz Applications,” *IEEE Photonics J.* , vol. 14, no. 5, pp. 1–8, 2022, doi: 10.1109/JPHOT.2022.3203509.
[32] H. Tao, N. I. Landy, C. M. Bingham, X. Zhang, R. D. Averitt, and W. J. Padilla, “A metamaterial absorber for the terahertz regime: design, fabrication and characterization,” *Opt. Express*, vol. 16, no. 10, p. 7181, 2008, doi: 10.1364/oe.16.007181.
[33] S. Ahmed *et al.*, “Enhanced structural tunability and high sensitivity of a THz metasurface absorber for precise automotive fuel characterization,” *Sci. Rep.*, vol. 15, no. 1, pp. 1–16, 2025, doi: 10.1038/s41598-025-05326-0.
[34] N. I. Landy, C. M. Bingham, T. Tyler, N. Jokerst, D. R. Smith, and W. J. Padilla, “Design, theory, and measurement of a polarization-insensitive absorber for terahertz imaging,” *Phys. Rev. B - Condens. Matter Mater. Phys.*, vol. 79, no. 12, pp. 1–6, 2009, doi: 10.1103/PhysRevB.79.125104.
[35] H. Ge *et al.*, “Tri-band and high FOM THz metamaterial absorber for food/agricultural safety sensing applications,” *Opt. Commun.*, vol. 554, no. November 2023, 2024, doi: 10.1016/j.optcom.2023.130173.
[36] A. Veeraselvam, G. N. A. Mohammed, K. Savarimuthu, and P. D. Vijayaraman, “An Ultra-Thin Multiband Refractive Index-Based Carcinoma Sensor Using THz Radiation,” *IEEE Sens. J.*, vol. 22, no. 3, pp. 2045–2052, 2022, doi: 10.1109/JSEN.2021.3134663.
[37] X. J. Liang, A. Q. Liu, C. S. Lim, T. C. Ayi, and P. H. Yap, “Determining refractive index of single living cell using an integrated microchip,” *Sensors Actuators, A Phys.*, vol. 133, no. 2 SPEC. ISS., pp. 349–354, 2007, doi: 10.1016/j.sna.2006.06.045.
[38] W. J. Choi, D. I. Jeon, S.-G. Ahn, J.-H. Yoon, S. Kim, and B. H. Lee, “Full-field optical coherence microscopy for identifying live cancer cells by quantitative measurement of refractive index distribution,” *Opt. Express*, vol. 18, no. 22, p. 23285, 2010, doi: 10.1364/oe.18.023285.
[39] P. Upender and A. Kumar, “Ultrathin, Ultra Narrow Band DMMA for Biosensing Applications,” *IEEE Trans. Nanobioscience*, vol. 22, no. 3, pp. 529–537, 2023, doi: 10.1109/TNB.2022.3217077.
[40] N. Ayyanar, G. Thavasi Raja, M. Sharma, and D. Sriram Kumar, “Photonic Crystal Fiber-Based Refractive Index Sensor for Early Detection of Cancer,” *IEEE Sens. J.*, vol. 18, no. 17, pp. 7093–7099, 2018, doi: 10.1109/JSEN.2018.2854375.
[41] M. Nejat and N. Nozhat, “Ultrasensitive THz Refractive Index Sensor Based on a Controllable Perfect MTM Absorber,” *IEEE Sens. J.*, vol. 19, no. 22, pp. 10490–10497, 2019, doi: 10.1109/JSEN.2019.2931057.
[42] H. Zhang, C. Liu, C. Xu, Z. Li, Y. Wang, and Y. Peng, “A dual-band terahertz metamaterial sensor with high Q-factor and sensitivity,” *Opt. Quantum Electron.*, vol. 55, no. 13, pp. 1–16, 2023, doi: 10.1007/s11082-023-05456-7.
[43] S. Singh and S. P. Singh, “Wide incidence angle-polarization insensitive multiband terahertz metamaterial biosensor for early-stage cancer detection,” *Opt. Quantum Electron.*, vol. 57, no. 9, pp. 1–23, 2025, doi: 10.1007/s11082-025-08414-7.
[44] H. M. Mamoun, M. F. O. Hameed, O. Hatem, S. T. Assar, S. S. A. Obayya, and M. Y. Azab, “Design of Highly Sensitive Dual-Band THz Metamaterial Sensor for Cancer Early Detection,” *Plasmonics*, vol. 20, no. 12, pp. 11057–11073, 2025, doi: 10.1007/s11468-025-03161-7.